1

Advanced UAV Aerodynamics, Flight Stability and Control: An Introduction

Pascual Marqués

Marques Aviation Ltd, Southport, UK

'For some years I have been afflicted with the belief that flight is possible to man.'
Wilbur Wright, 13 May 1900.

This introductory chapter is divided into two main sections: Section 1.1 on unmanned aircraft aerodynamics and Section 1.2 on flight stability, and control. The chapter addresses fundamental principles of aerodynamics, flight stability and control and forms a knowledge base for the student of aerospace engineering before proceeding to more advanced chapters in this book. The chapter includes classroom problems.

1.1 Unmanned Aircraft Aerodynamics

1.1.1 Introduction: UAV Categories and Configurations

Unmanned aerial vehicle (UAV) size categories range from nano air vehicles (NAV) with a wing span of only 4 cm to high-altitude long-endurance (HALE) aircraft with a wing span of 35 m or more. In between, UAV categories include micro (MAV), mini, close-range, medium-range or tactical and medium-altitude long-endurance (Figure 1.1). The fluid medium in which an NAV operates is highly viscous, whereas the fluid flow around large (normally manned) aircraft is dominated by inertial effects. Consequently, aerodynamic characteristics vary considerably according to the size of the vehicle.

The aeronautical configuration of a UAV is closely related to its operational mission requirements and dictated by airspeed, endurance and operational range. Whether the vehicle is fixed-wing or rotary-wing is determined by the speed requirements. HALE surveillance aircraft necessitate a high aspect ratio (AR) wing for flight at high altitude. In contrast, Unmanned Combat Air Vehicles (UCAVs) operate at high airspeed and perform rapid manoeuvers and therefore have low AR wings. Civilian or military applications that involve operation from off-board a ship benefit from vertical take-off and

Advanced UAV Aerodynamics, Flight Stability and Control: Novel Concepts, Theory and Applications,
First Edition. Edited by Pascual Marqués and Andrea Da Ronch.

Companion website: http://www.wiley.com/go/marques/advanced_UAV_aerodynamics

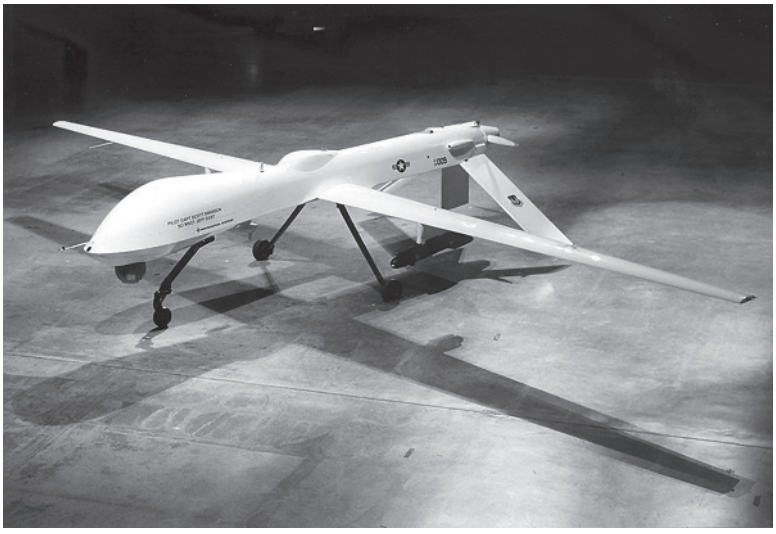

Figure 1.1 General Atomics RQ-1A Predator. (Photo: USAF Museum). (*See insert for color representation of this figure.*)

landing capability of the aircraft. Fixed-wing configurations include *tailplane aft*, *tailplane forward* or *canard*, and *tailless* types.

The conventional tailplane aft designs usually have the horizontal stabiliser positioned aft on the fuselage or connected to the wings by booms. The aircraft's centre of gravity (CG) is often forward of the aerodynamic centre (AC), which creates a nose-down pitching moment. To this negative moment must be added the nose-down moment characteristic of cambered wings. The net nose-down moment is balanced by a down-load on the tailplane.

In a canard configuration, both the foreplane and the CG are located forward of the wing. Equilibrium in pitch is achieved by the positive lift generated by the foreplane. The canard design is aerodynamically more efficient than the tailplane aft design, as both the horizontal stabiliser and the wing produce positive lift.

Tailless types include the flying wing and delta configurations. Tailless types have sweptback wings and an effective tail. The airfoils at the wingtips are set at a lower incidence than the airfoils of the inner wing, in a washout configuration to provide stability in pitch. The absence of a horizontal stabiliser reduces profile drag. However, wing sweepback in the flying wing leads to poor lift distribution, high induced drag and negative lift at high airspeeds. Delta wings have a low AR, poor lift distribution and higher induced drag caused by high span loading.

In the majority of UAVs, the powerplant is mounted at the rear of the fuselage. This arrangement makes the front of the aircraft available for the installation of a payload and allows an unobstructed view forward. There are also aerodynamic advantages when using a rear-mounted propeller. The friction drag induced by the slipstream ahead of the pusher propeller is less than the drag generated by a front-mounted tractor propeller. Ubiquitous types of rotary-wing UAVs are the *single-main rotor* and *quad rotor* (Figure 1.2). Other alternatives in design are the *co-axial rotor* and *hybrid* configurations such as the *tilt-rotor* and *tilt-wing*.

Figure 1.2 Aeryon Scout VTOL MAV with gyro-stabilized camera payload. Photo: Dkroetsch CC-BY-3.0.

1.1.2 Theoretical Aerodynamics

Aerodynamic analysis of novel concepts in UAV design can be conducted using a number of methodologies that range from traditional aerodynamic theories to modern computational fluid dynamics (CFD). *Thin-airfoil theory* is an analytical method that predicts lift as a function of angle of attack and assumes idealised incompressible inviscid flow. The theory can be applied to airfoils of thickness no greater than 12% of the chord (c) at low angles of attack (below the stall). Thin-airfoil theory was developed by German–American mathematician Max Munk and further refined by British aerodynamicist Hermann Glauert in the 1920s. The theory provides a sound theoretical foundation for modern aerodynamic theories. Prandtl's *lifting-line theory* is a mathematical model for the prediction of the lift distribution along the span of a three-dimensional wing (Figure 1.3). In the model, the vortex strength varies elliptically along the wingspan and the loss in vortex strength is shed as a vortex-sheet from the trailing edge. Lift distribution is obtained from the wing geometry (constituent airfoil, taper, twist) and freestream conditions; that is, air density and flow velocity. Modified versions of the classical lifting-line theory are used to compute the lift distribution in geometrically- or aerodynamically-twisted wings.

The *vortex panel method* is a numerical method that permits the computation of airfoil lift assuming ideal flow in which the effects of compressibility and viscosity are negligible. In this method, the shape of the airfoil surface is reconstructed using a series of vortex panels or line segments arranged to form a closed polygon. Vortex sheets mimic the boundary layer around the airfoil. The vortex sheets represent miniature vortices that give rise to circulation, hence lift.

1.1.3 Flight Regimes and Reynolds Number

The Reynolds number (Re) is a dimensionless number that indicates the ratio of inertial forces to viscous forces for given flow conditions. The concept is named after Osborne Reynolds who introduced its use in 1883. The Re characterizes different flow regimes.

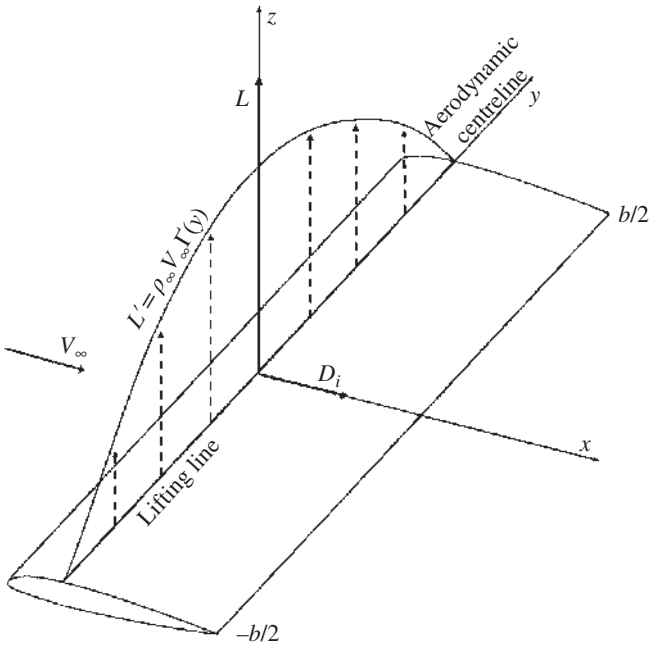

Figure 1.3 Prandtl's classical lifting-line theory. L', lift per unit span; ρ_∞, air density; V_∞, freestream velocity; $\Gamma(y)$, circulation; D_i, induced drag.

Laminar flow occurs at low Res, where viscous forces dominate. Turbulent flow occurs at high Res where inertial forces predominate. Small UAVs operate in the Re regime between 3×10^4 and 5×10^5. For operation at low Re, the design of efficient airfoils is critical. At $3 \times 10^4 \leq \mathrm{Re} \leq 7 \times 10^4$, relatively thick airfoils (≥6% thickness) can experience considerable hysteresis as a result of the lift and drag forces caused by laminar separation and transition to turbulent flow. Below Re values of 5×10^4, laminar separation occurs and the flow does not transition and it does not reattach to the airfoil surface. At $7 \times 10^4 \leq \mathrm{Re} \leq 2 \times 10^5$, extensive laminar flow over the surfaces of the airfoil can be attained, which reduces airfoil drag. However, in some airfoils a laminar separation bubble forms in this flight regime. At Re values above 2×10^5, airfoils become more efficient. The bubble is shorter and parasite drag decreases. The flight regime of large UAVs is in the region of $\mathrm{Re} \geq 3 \times 10^6$. At high Re values, the laminar boundary layer transitions to turbulent a short distance downstream of the wing's leading edge. Laminar separation and separation bubbles do not occur.

1.1.4 Airfoils for UAVs

The cost of operation of a UAV can be reduced with airfoil optimization and improvements in the vehicle's aerodynamic efficiency. Considerations when selecting an airfoil for a UAV include a high maximum lift coefficient ($c_{l\max}$), high lift-to-drag ratio (c_l/c_d), high endurance factor ($c_l^{3/2}/c_d$), effectiveness at low Re values, low pitching moment coefficient to minimize the load on the tail, mild stall characteristics, insensitivity to surface roughness caused by rain or dust, good flap performance, and minimal airfoil

complexity for ease of manufacture. Airfoils originally designed for operation at high Re for manned aircraft ($3 \times 10^6 \leq \mathrm{Re} \leq 6 \times 10^6$) are often adapted for UAVs that operate in the low-Re flight regime (e.g., $5 \times 10^5 \leq \mathrm{Re} \leq 1.5 \times 10^6$). The aerodynamic performance of airfoils operating in off-design conditions of low Re deteriorates proportionally to the reduction in Re, manifested as a lower $c_{l\max}$, higher drag, worsened c_l/c_d, and possible lift coefficient (c_l) hysteresis behaviour as the airspeed and Re fluctuate during flight. Hysteresis is caused by the bursting of the laminar separation bubble at low Re values. Therefore, when adapting an airfoil for a small UAV it is important to examine the aerodynamic performance and hysteresis of the airfoil in the off-design low-Re flight regimes in which the vehicle will operate.

An example of an airfoil adapted for small UAVs is the Selig Donnovan SD7032 (Figure 1.4, top). The relatively simple geometry of this airfoil makes wing manufacture uncomplicated. The SD7032 has a $c_{l\max}$ of 1.5, and lower drag than the early-design NACA 23012, of similar geometry. The SD7032 performs well at low Re values through the full range of values of c_l.

Designed for extensive laminar flow over both the upper and lower surfaces, the Wortmann FX61-147 (Figure 1.4, centre) has a thickness ratio of 14.7%, camber of 3.18% and $c_{l\max}$ of 1.5 (Reneaux *et al*., 1997). Its considerable thickness allows the low drag bucket to be maintained for a large range of values of c_l. However, the large airfoil thickness incurs a higher minimum drag coefficient. At relatively low flight speeds (say,

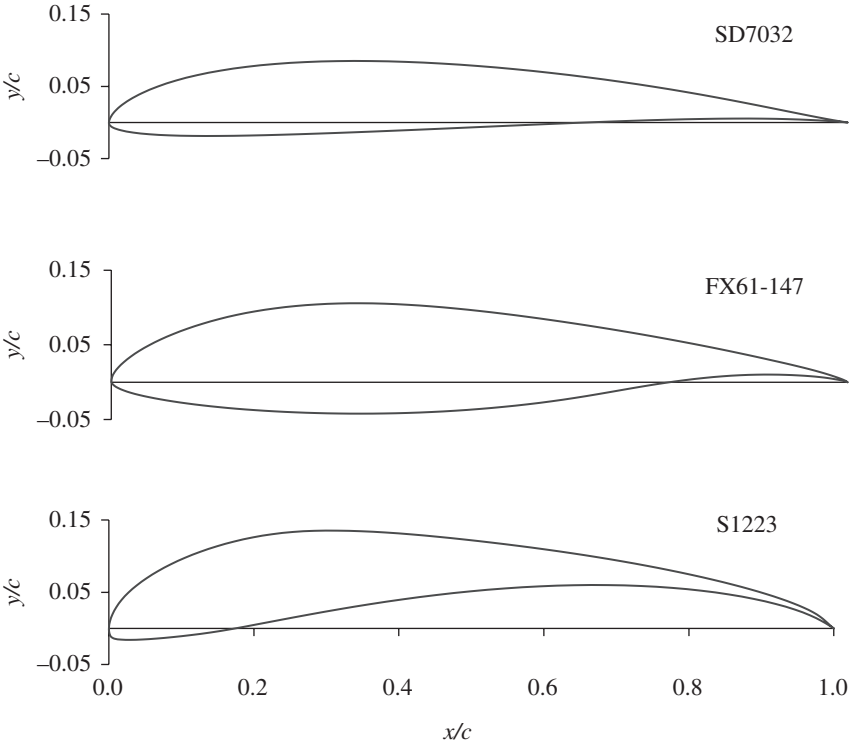

Figure 1.4 Airfoil coordinates.

a low Re of 1.5×10^6), this airfoil generates low drag due to its extensive laminar flow characteristics. Transition of the boundary layer from laminar to turbulent is caused by laminar separation bubbles. At high values of c_l, the finite transition region moves upstream on the upper surface and at low values of c_l a loss of laminar flow occurs in the lower surface. The FX61-147 performs fairly well in small UAVs. Nonetheless, attention need to be paid to the movement of the finite transition region towards the leading edge and the extent of the laminar separation bubble with fluctuations in flight speed and the associated hysteresis.

The S1223 airfoil (Figure 1.4, bottom) of 12.1% thickness ratio and 8.9% camber is a popular choice for small UAVs (Ma *et al.*, 2010). This airfoil emerged from the high-lift design philosophy, which is characterised by concave pressure recovery with aft loading. At the low Re of 1.5×10^5, the S1223 exhibits a c_{lmax} of 2.2, high c_l/c_d and acceptable stall characteristics. Higher values of c_l are achieved with the installation of vortex generators on the upper surface located at 17% c and also through the use of a Gurney flap. However, the high camber and complex shape of the S1223 makes wing manufacture intricate and more expensive. High lift is essential for UAVs that operate at low speeds with the wing near the c_{lmax} for loitering, cruising and landing. The S1223 has a high c_{lmax}, which is approximately 25% higher than for an FX63-137 airfoil. The S1223 also shows good flight performance compared with the NACA 0012 and CLARK-Y, thus implying that a high cambered airfoil is preferable. The higher lift of the S1223 incurs a drag penalty, but a better c_l/c_d ratio can be obtained using airfoil optimization. Because of their inherent laminar boundary layer, low-Re airfoils have low skin-friction drag. Optimization of the low-Re S1223 airfoil involves preserving low-friction drag by modifying both the upper and lower surfaces and delaying transition (Ma *et al.*, 2010). Optimization using CFD has resulted in the S1223 OPT 2 airfoil, which shows increased lift and efficiency, and therefore good aerodynamic characteristics in off-design conditions. At low values of Re ($7.5 \times 10^4 \leq \text{Re} \leq 2.0 \times 10^6$), increased camber and reduced thickness provide more favourable lift, drag and endurance factor characteristics. A flexible airfoil, such as the UF airfoil of 6% thickness and 8.9% camber, yields better overall performance than a similar rigid profile in the unsteady oscillating environment characteristic of turbulent flight conditions (Shyy *et al.*, 1999).

1.1.5 Wing Geometry

Induced drag is caused by the wingtip vortex and it is a by-product of the lift force generated by the wing. Wings with higher AR yield less induced drag and enhance UAV flight efficiency. The lift force generated by a wing is a function of several parameters: the constituent airfoil, wing geometry, air density, airspeed and angle of attack. The UAV designer must consider the different planform shapes and evaluate the spanwise lift distribution of each variant. The wing planform of a UAV can be rectangular, elliptical, straight tapered, sweptback, sweptback tapered, semi tapered, forward swept tapered, delta, double delta, crescent, ogival, blended wing-body, joined, or some other shape (Figure 1.5). A wing of elliptical planform is the most efficient. It produces a constant lift distribution along the span and minimum induced drag. However, a purely elliptical wing is difficult to build. A rectangular planform is uncomplicated to construct, but the wingtips are 'idle' - they generate little lift. The rectangular planform has the advantage that the wing root stalls before the wing tips. Thus, aileron function is

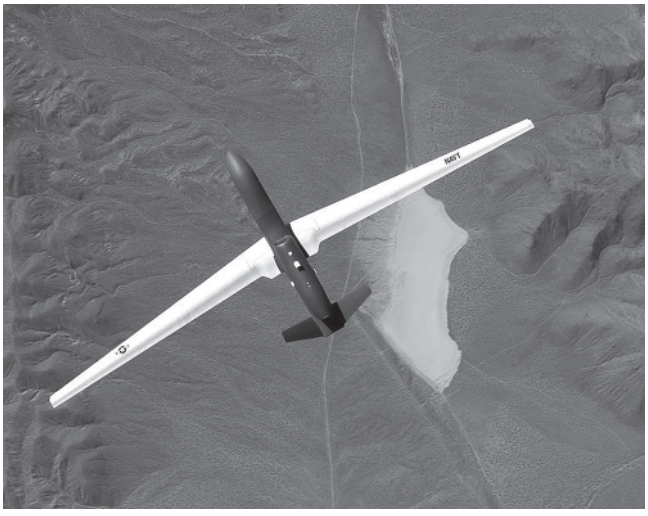

Figure 1.5 Sweptback tapered planform in a Northrop Grumman RQ-4 Global Hawk. Photo: Jim Gordon.

maintained, as the ailerons are positioned outboard on the wing. A practical compromise is to use a straight wing that is tapered towards the tip; this improves the spanwise lift distribution. In a sweptback tapered planform, the c_l increases gradually towards the wingtip. Such increasing lift distribution is even more prominent in the delta and double-delta planforms. The tips tend to stall at a lower angle of attack than the wing root, which is undesirable in aircraft. Aileron function deteriorates, and the UAV tends to drop one wing and possibly enter a spin from which the vehicle is difficult to recover.

Tip stall in sweptback-tapered, delta and double-delta wings is prevented by twisting the wing in a washout configuration, so that the wing tips are set at a lower angle of incidence than the wing root. Geometric and/or aerodynamic twists is employed in UAVs to reduce the strength of the tip vortex and the associated induced drag, control the stall so that the wing root stalls first, and maintain aileron function. Improved wing performance is attained using an optimised amount of total twist together with an optimised elliptical distribution of the twist along the span. The work of Boschetti *et al.* (2012) has shown that application of local twist near the wingtip region is also effective in reducing induced drag. Phillips (2005) has developed an adaptive control surface, the twisteron, which modifies the shape of the tailing edge of the wing in response to instantaneous flight conditions to maximize lift and diminish induced drag.

1.1.6 Wingtip Devices

The strength of the wingtip vortices, downwash and induced drag are reduced using winglets (Azlin *et al.*, 2011). Winglets increase the effective AR of the wing. The use of winglets is often dictated by aircraft aesthetics. While the winglets are intended to restrict the tip vortex, it is difficult to prove their effectiveness in practice. Induced drag is inversely proportional to the square of the freestream velocity. Therefore, reducing vortex drag is important during slow flight, and when the angle of attack and values of c_l are high. There is little vortex drag to be saved at high speed. Thus, winglets create

additional parasite drag at high flight speeds. The Whitcomb winglet is a carefully designed tip device that extracts some of the energy from the wingtip vortex. The device weakens the tip vortex and turns energy into forward propulsion. However, the Whitcomb winglet has several limitations. The precise angle of attack of the winglet changes as the strength of the wingtip vortex varies with flight speed and wing angle of attack. The winglet is efficient for only a narrow range of flight speeds. Nonetheless, UAVs operate mostly at one speed and optimisation of the winglet is possible, although winglet optimisation requires extensive research. Most of the winglet lift acts laterally, which tends to bend the winglet and add load to the wing structure. The lift generation produces localised vortices and therefore vortex drag at the tips of the winglets. The use of winglets for applications in UAVs is an area that requires further research. Wingtip fences, raked wingtips, non-planar wingtips, upswept tips, Hoerner tips, and tip sails offer appealing alternatives in UAV design.

1.1.7 High-lift Devices

Multi-element wings increase the maximum lift coefficient of the wing during takeoff and landing. Multi-element systems consist of movable leading- and trailing-edge devices such as the Krueger flap and the Fowler flap, respectively. At high wing angles of attack, slotted Krueger flaps allow the higher pressure on the underside of the slat to travel through the slot, gaining velocity and energising the boundary layer over the upper wing surface. There are different categories of trailing-edge flap systems, which vary in complexity; these include plain, split, slotted and Fowler flaps. The plain flap is the most common in UAVs due to its simplicity. A split flap yields greater increases in lift, but it creates more drag and is costlier to construct. In a slotted flap, airflow from under the wing passes through the gap between the main wing element and the flap and energises the turbulent boundary layer over the upper surface of the flap. This leads to better boundary-layer adherence, and allows a larger angle of attack before the stall, a higher c_l and lower drag than the plain flap. Deflection of a Fowler flap entails rearward extension of the flap, which increases both the wing area and camber. The Fowler flap yields generous gains in lift, but it is mechanically complex and difficult to construct. Flaperons incorporate a flap for high lift and an aileron for roll control in the same control surface. The flaperon is not integral with the wing but it is attached to the underwing and acts like an external wing flying in close formation with the main wing. A flaperon can increase c_l by 1.0 but adds a drag penalty. Elevons contain the elevators and ailerons on the same mechanical control to provide combined pitch and roll control.

With reduced UAV flight speed and increasing angles of attack during the approach to landing, the boundary layer becomes unstable and tends to separate. The boundary layer can be energised using a vortex generator. These small vanes are of rectangular or triangular shape and are positioned obliquely at an angle of attack with respect to the local airflow. Each vane creates a tip vortex. Vortex generators have a height of 80% of the boundary-layer height and draw energetic rapidly-moving air from outside the slow-moving boundary layer into contact with the aircraft skin. They delay flow separation and stall, and improve the effectiveness of the control surfaces.

Gurney flaps are mechanically-simple but highly-effective devices that increase the maximum lift of the wing, vertical fin or horizontal stabiliser. The Gurney flap is a small flat tab of a height of 1–2% of c. The flap projects from the trailing edge, at right angles to the

pressure side, and runs along the full span of the lifting surface. The underlying principle behind the Gurney flap is that it improves the aerodynamic performance of the constituent airfoil. The flap increases the pressure on the pressure side and reduces the pressure on the suction side. The boundary layer remains attached at the trailing edge on the suction side.

1.1.8 Aeroelasticity

Aircraft performance is influenced by aeroelastic phenomena, arising from the interaction of elastic, inertial and aerodynamic forces. There is a strong link between aeroelasticity and loads. UAV structures are not completely rigid. Aeroelastic phenomena occur when structural deformations cause changes in aerodynamic forces. The additional aerodynamic forces further increase the structural deformations, which lead to greater aerodynamic forces in a self-feeding fashion. These interactions may attenuate until a condition of equilibrium is reached, or may diverge catastrophically as a result of resonance.

Aeroelasticity can be categorised as *steady* (*static*) or *dynamic*. Steady aeroelasticity involves the interaction between aerodynamic and elastic forces on an elastic structure. Phenomena studied under the category of steady aeroelasticity include *divergence* and *control surface reversal*. Divergence occurs when a lifting surface deflects under an aerodynamic load. The applied load increases and the twisting effect on the structure intensifies. The increased load deflects the structure further, eventually bringing it to its load limit and to failure. Control surface reversal is the loss (or reversal) of the expected response of a control surface due to structural deformation of the main lifting surface. Examples of dynamic aeroelastic phenomena include flutter, dynamic response and buffeting. Flutter is a self-feeding and potentially destructive form of vibration where aerodynamic forces on an object couple with a structure's natural mode of vibration to produce rapid periodic motion. When the energy input by the aerodynamic excitation is larger than that dissipated by damping in the system, the amplitude of vibration will increase, resulting in a self-exciting oscillation. Dynamic response is the response of the UAV to gusts and atmospheric disturbances. Buffeting is defined as high-frequency instability caused by airflow separation or shock wave oscillations from one object striking another. It is a random forced vibration. Generally, it affects the tail unit of the aircraft structure due to the wake downstream of the wing.

Trailing edge micro-actuators can facilitate the aeroelastic control of a UAV by providing flutter suppression in a flexible wing (Kroo *et al.*, 2003). Aeroelastic problems can be solved by stiffening the structure or altering mass distribution. However, such methods incur a performance penalty. For UAVs, active control of the aeroelastic behaviour is the best solution. Actuator technology makes use of small devices that are capable of generating forces sufficient for aeroelastic control. Small simple trailing-edge devices do not require accurate servo control. For example, the Miniature Trailing Edge Effector (MiTE) consists of a large number of micro devices of a height of 1–5% of c that deploy along the wing span and are deflected vertically into the flow. Their operation is similar to that of a Gurney flap.

1.1.9 Helicopter and Quad Rotor UAVs

Current trends in rotorcraft UAV design include vibration and noise reduction, rotor performance improvement, active blade tracking, and stability augmentation. Helicopter UAVs can be affected by a number of problems, including high vibratory loads, noise

generation, poor performance, instabilities, difficulties in maintaining rotor-blade track, and limited load capacity and forward flight speeds (Wilbur and Wilkie, 2005). These problems originate from the highly variable aerodynamic environment that the rotor system encounters as it rotates in forward flight. The normal approach to eliminating these problems has been to modify the periodic aerodynamic loads. The simplest method is to modify the rotor-blade pitch at harmonic frequencies above the rotational frequency of the rotor.

Higher harmonic control reduces vibration and noise through use of active control of the rotor swashplate to change the pitch at the root of the blades. Another active control method, known as individual blade control (IBC) uses hydraulically actuated pitch links to achieve control of each of the blades independently. A concern when using IBC is obtaining the necessary hydraulic power in the rotating system. Current active rotor-control concepts include on-blade controls, such as trailing-edge flaps or strain-induced blade twist actuated by piezoelectric devices. On-blade active control is a feasible and efficient approach to solving rotor-system problems. Nonetheless, active rotor-control systems can be complex, expensive to develop, and bring inherent risks when implemented in a vehicle that will carry human beings. A recommended approach for the successful development of such technologies is experimentation using UAVs. Active-twist helicopter rotor systems have been explored recently. This type of rotor uses piezoelectric fiber composite actuators embedded within the composite blade structure. When excited by an electrical voltage, the actuators produce strain-induced twisting motions of the blade. Test results indicate that significant vibration and noise reduction can be achieved.

Small quad rotors have an important role in civil and military operations. A quad rotor is a vertical takeoff and landing (VTOL) air vehicle that can travel omni-directionally and also hover. The vehicle is powered by four motors attached to a rigid cross frame (Sanchez *et al*., 2011). Quad rotor control is achieved by varying the rotational speed of the rotors. Each rotor produces combined thrust and torque that generate the main pitch, roll and yaw movements of the rotorcraft. The front and rear rotors rotate counter-clockwise, while the left and right rotors rotate clockwise, thus cancelling gyroscopic effects and aerodynamic torques in stationary trimmed flight. Vertical motion is controlled using collective throttle input. Forward and backward motion is achieved by adjusting the differential speed of the front and rear motors, which causes the quad-rotor to tilt at a pitch angle. Left and right flight is accomplished by controlling the differential speed of the right and left motors, tilting the craft at a roll angle. The two sets of rotors turning in opposite directions permit yawing of the vehicle. Yaw rotation is attained by increasing or decreasing the speed of the front and rear motors while also adjusting the speed of the lateral motors (Figure 1.6). The total thrust is kept constant to maintain altitude. Most designs use fixed-pitch propellers that are controlled by individually varying the rotational speed of each of the four rotors. Future variable-pitch designs could increase the operational envelope of the quad rotor. In fact, blade-element numerical codes are able to capture the effects of the blade geometry and forward flight to explore variable-pitch capability.

1.1.10 Adaptive Wing Technology

Aircraft wings represent a compromise that will allow the aircraft to fly in different conditions. However, the aircraft's aerodynamic performance in each condition is sub-optimal (Barbarino *et al*., 2011). Adaptive wings change their geometry during flight to

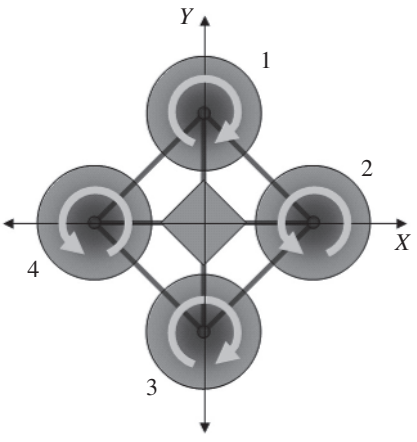

Figure 1.6 Yaw torque and control in a quad rotor aircraft. Rotors 1 and 3 spin in one direction and rotors 2 and 4 spin in the opposite direction, yielding opposing reaction torques. Image: Gabriel Hoffmann.

optimise the wing configuration. Geometrical parameters susceptible to morphing include: airfoil (camber and thickness), planform (chord, span, sweep), and out-of-plane (twist, dihedral/gull, span-wise bending). Modern smart materials allow the blending of morphing and smart structures for the design of the next generation of UAVs.

The morphing wing is a biomimetic technology that has been applied to UAVs by means of changes in wing cross-section, planform, and spar position. Yang *et al.* (2006) investigated a morphing wing with variable camber using shape memory alloy (SMA) actuators. SMAs have the unique effects of shape memory and pseudoelasticity, which result from phase transformations between martensite (rapid cooling) and austenite (heating) phases induced by changes in temperature or applied stress. SMAs allow high recovery forces and large deformations. Lift force increases without a parallel increase in drag. Monitoring of aeroelastic unstable phenomena at various angles of attack reveals limit-cycle oscillations with constant frequency at flutter speed. Activation of the SMA actuators considerably reduces the amplitude of the limit-cycle oscillations. Such findings suggest that a smart composite wing with integrated smart sensors and actuators is feasible for applications in UAVs and MAVs with relatively simple and less stiff wing structures. Gamboa *et al.* (2007) present a morphing approach for wing-drag reduction in small UAVs. A tool is used that searches for an optimum airfoil geometry and wing planform shape, given geometric wing constraints. The aerodynamic analysis consists of two stages. First, the two-dimensional aerodynamic coefficients based on angle of attack and Re are obtained using the airfoil flow field solver XFOIL (an interactive program for the design and analysis of subsonic isolated airfoils). Instead of using control points to define the airfoil surface, control points are used to represent the airfoil camber line and thickness distribution. Second, a non-linear lifting-line-method algorithm gives the lift distribution and induced drag. Aerodynamic shape optimization is carried out using the sequential quadratic programming constrained optimization algorithm DONLP2. Computational analysis shows that 14–30% drag reduction is attainable at different stages of flight. A novel gust-load alleviation technique based on active flow control was developed by Xiaoping *et al.* (2011). The dynamic response of the quasi 'Global Hawk' airfoil was investigated using arrays of jets during gust simulation based on the unsteady Navier–Stokes equations. Five kinds of flow-control technique were introduced, including steady blowing, steady suction, unsteady blowing, unsteady

suction and synthetic jets. Physical analysis of the effect on gust-load alleviation was then used to produce new guidelines for practice. The numerical results showed that a new technique called 'active flow-control' could effectively suppress gust-induced fluid disturbances.

Planform morphing aims to emulate nature in aerial vehicles, enabling highly adaptive and fluidic motions with freedom of configuration (Barbarino *et al*., 2011). The concept of morphing aircraft dates back to the Wright brothers' first powered aircraft. To control the vehicle, the pilot shifted his hips, which in turn actuated tendons that twisted the wings. The concept of 'wing-warping' was soon abandoned and today most aircraft use conventional hinged control surfaces. Planform morphing is used for mission adaptation, and control morphing allows vehicle manoeuvring. Planform morphing involves varying wingspans, sweeps and tail configurations such that the AR, planform area and static margin are modified. Control morphing involves smaller changes that alter the flowfield slightly, enabling the aircraft to manoeuvre, but without significantly affecting its dynamics. Combinations of planform and control morphing permit advanced manoeuvring capabilities; for example, using wing twist and asymmetric wing extension for effective roll control.

1.1.11 Hybrid Aircraft

Fixed-wing UAVs are able to fly for long periods at high speeds and their mechanical design is relatively simple. However, they require runways or additional launch and recovery equipment. Rotary-wing UAVs do not need forward airspeed for flight and manoeuvring, and do not require any infrastructure for takeoff and landing. However, rotary wing UAVs are mechanically complex and have low flight speeds and endurance. Hybrid UAVs integrate both horizontal and vertical flight capabilities. They are, however, more mechanically complex and more difficult to control. Tilt-rotor UAVs possess adequate stability, energy efficiency and controllability. Examples of UAV's with dual tilt-rotors include the Bell Eagle Eye, the Smart UAV of KARI and the BIROTAN, while UAVs with dual tilt-wings include the HARVee and the UAV of the Universita di Bologna. The dual-rotor UAVs require cyclic controls on the propellers for stabilization and manoeuvring, and are thus more complex. Electric-powered quad tilt-wing UAVs are capable of VTOL in addition to horizontal flight (Cetinsoy *et al*., 2012). Greater stability is attained with a quad tilt-wing UAV, such as the QUX-02 of the Japan Aerospace Exploration Agency.

The aerodynamic design of the quad tilt-wing UAV developed by Cetinsoy *et al*. (2012) aims to generate sufficient lift for flight while minimizing drag. The fuselage shape is a rectangular prism with rounded nose and back sections, and gradually decreasing thickness for streamlining. When viewed from the top, the fuselage resembles a symmetrical wing. This water-drop shape gives a low drag coefficient. The wing planform is adjusted by considering the speed range, wing-span constraints, wing efficiency and interactions with the fuselage. Airfoil chord length, maximum camber ratio and thickness were determined using simulations in the ANSYS® environment. The slipstream velocity from the rotors needs to be taken into account, since the rotors have a marked effect on the behaviour of the wings. The use of greater chord lengths and large winglets, instead of greater wing thickness, increases efficiency. In fact, at high angles of attack, the large chord provides a large inclined surface against the air flow. At high speeds, a thicker wing causes greater drag. It is known that thin wings with low camber experience leading-edge

separation at lower angles of attack, which leads to stalls. However, the wings of the quad tilt-wing UAV are almost fully submerged in the slipstream of the propellers and the high-speed slipstream prevents air separation at high angles of attack and gives additional lift. The low AR of 4 and the rectangular planform cause severe spanwise airflow at high angles of attack. The spanwise airflow reduces wing aerodynamic efficiency due to strong wingtip vortices and pressure equalization in the wingtip region. The large winglets restrict the tip vortex. The lift of the rear wings is adversely affected by the downwash of the front wings. This causes imbalances in the transition and horizontal flight modes as the centre of mass of the vehicle is located between the aerodynamic centres of the front and rear wings. The downwash from the two front wings reduces the effective angle of attack of the rear wings. To account for the downwash configuration, the rear wings are set at a higher angle of incidence.

1.1.12 Transonic and Supersonic Flight Regimes

The behaviour of supersonic airflow is very different to that of subsonic flow. In front of a UAV, the fluid builds up a stagnation pressure as its impact with the vehicle brings the moving fluid to a rest. At subsonic speeds, the pressure disturbance propagates upstream, changing the flow pattern ahead of the aircraft. At supersonic speeds, the pressure disturbance does not propagate upstream and when the airflow strikes the front of the UAV, it is forced to change its properties (temperature, density, pressure, and Mach number) in a violent and irreversible fashion, producing a shock wave. At flight speeds near the speed of sound, supersonic flow and wave drag may occur over parts of the wing. Wave drag is considerably higher than induced drag, and must be avoided to improve UAV performance. Wave drag is prevented using a very thin wing that has a slowly changing airfoil profile over a wide chord. Limitations of very thin wings include insufficient space for fuel storage and the landing gear, and less torsional stiffness. Wing sweep prevents the development of the shock wave at the leading edge (Figure 1.7).

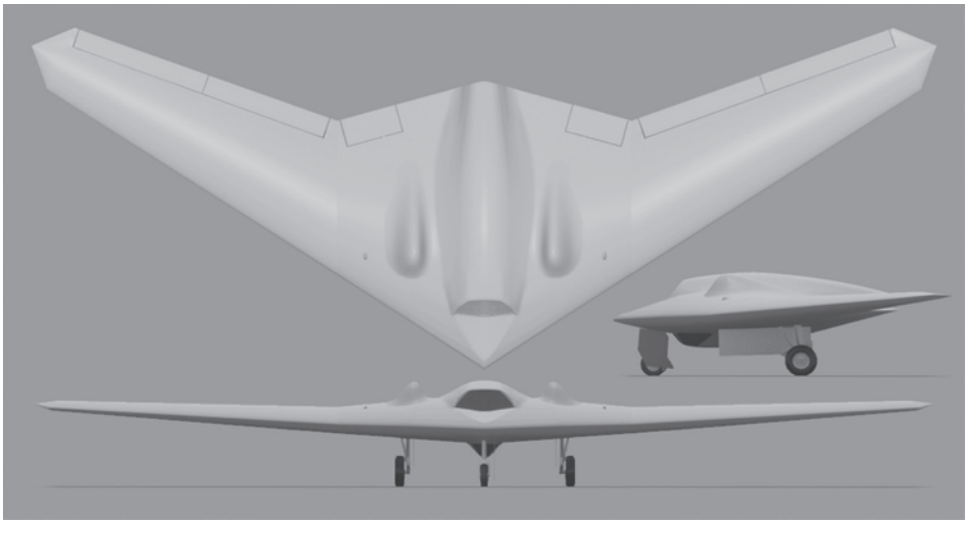

Figure 1.7 Pronounced wing sweepback in a Lockheed Martin RQ-170 Sentinel. Image: Truthdowser.

1.1.13 Wind Tunnel Testing and Computational Fluid Dynamics

There is a scarcity of airfoil experimental data at low values of Re. The use of wind tunnel testing to design and optimize new airfoils is time consuming and costly. With the emergence of high-speed electronic computers, numerical simulation is frequently used in airfoil design. CFD is an effective method of studying the complex flow field around the airfoil, allowing rapid evaluation of preliminary airfoil designs, and reducing cost, time and the need for multiple experiments. CFD consists of a combination of aerodynamic analysis and optimization of the airfoil geometry for a given set of constraints. To ensure good aerodynamic performance for a range of fight speeds and conditions, multi-objective optimization is preferable to single-objective optimization. Therefore, the aircraft is optimised for a selected airspeed while preserving good performance in other flight regimes. For example, the design of an efficient high-lift low-Re airfoil for UAV applications can be achieved using hierarchical multi-objective optimization that combines the direct search optimization algorithm EXTREM with XFOIL to determine aerodynamic performance (Park *et al.*, 2008). Airfoil shape optimization comprises four steps.

- Describe or parameterize the airfoil shape.
- Select an appropriate aerodynamic analysis method.
- Implementing an effective CFD optimization algorithm.
- Identify a suitable multi-objective optimization method.

Design optimization commences by selecting a baseline airfoil. The new airfoil may be represented in the computer programme by Eqs. (1.1) and (1.2).

$$y_{\text{upper}}(x) = y_{\text{ou}} + \sum_{7}^{k=1} c_k f_k(x) \tag{1.1}$$

$$y_{\text{lower}}(x) = y_{\text{ol}} + \sum_{7}^{k=1} c_{k+7} f_k(x) \tag{1.2}$$

where, y_{ou} and y_{ol} are the ordinates of the upper and lower surface of the base airfoil, respectively, k represents the number of design variables, c_k represents the design variables and f_k symbolises the shape functions. Three commonly used shape parameterization methods are the polynomial, the Hicks–Henne and the Wagner functions. The Hicks–Henne function is given by Eq. (1.3).

$$f_k(x) = \begin{cases} x^{0.25}(1-x)e^{-20x}, & k=1 \\ sin^3\left(\pi x^{e(k)}\right), & k>1 \end{cases} \tag{1.3}$$

where,

$$e(k) = \frac{log 0.5}{log x_k}, \quad 0 \le x_k \le 1. \tag{1.4}$$

During shape parameterization, a linear superposition method can be used and the coefficients of the Hicks–Henne function determine a new airfoil shape using the leading- and trailing edges of the baseline airfoil. XFOIL uses a linear-vorticity stream-function panel method coupled with viscous integral boundary-layer equations for the analysis of airfoils with free or fixed transition, separation bubbles, blunt trailing edges, and limited trailing-edge separation over a range of Re values and Mach numbers. The validity, versatility and ease of use of the XFOIL programme for the preliminary design of subsonic airfoils and quick estimation of transition locations has been extensively documented. The direct search optimization algorithm EXTREM used for aerodynamic shape optimization can be used effectively for solving the multi-variable constrained optimization problem, converges quickly and requires no derivation. Once an extremum of optimization is attained, the optimization process is completed using parabolic extrapolation. Multi-objective aerodynamic optimization of airfoil design is a complex engineering problem that requires a combination of common multi-objective optimization methods and empirical evidence for specific problems to achieve a satisfactory design. The use of genetic algorithms underlies the functioning of multi-objective optimization. A typical optimization problem is expressed mathematically by the algorithm:

$$\textit{Find } x = \left\{ x_1, x_2, \ldots, x_m \right\}^T$$

$$\textit{to maximize } f_1(x) = c_l$$

$$\textit{to maximize } f_2(x) = c_l / c_d$$

$$\textit{to minimize } f_3(x) = c_{m,1/4}$$

$$\textit{subjected to } x_i^{\mathrm{L}} \le x_i \le x_i^{\mathrm{U}} \quad \textit{for } i = 1 \sim 13 .$$

where, $c_{m,¼}$ is the pitching moment about the quarter chord coefficient, and x_i^{L} and x_i^{U} are the upper and lower bounds of the design variables (Park *et al*., 2008).

Numerical methods reduce the cost and effort for the preliminary configuration of aircraft and enable the expansion of the flight regime to be analysed well beyond the technical capabilities of a wind tunnel. Calculated results can be validated to confirm their accuracy. For example, Tornado is an open-source three-dimensional vortex-lattice program written in MATLAB® that can be used to model 3D wing surfaces and calculate aerodynamic forces and coefficients and flight-stability derivatives for UAV design optimization. The vortex-lattice method represents the wing as a planar surface broken into quadrilateral panels on which a horseshoe vortex is superimposed. The law of Biot–Savart is used to calculate the velocities induced by each horseshoe vortex and the vortex strength at a specific control point. Vortex strength is related to the circulation around the wing and the pressure differential between the upper and lower surfaces. Aerodynamic forces are obtained by integration of the pressure differentials. Longitudinal flight stability derivates computed with Tornado have been shown to be in good agreement with experimental data, and lateral-directional derivates are acceptable (Cardenas *et al*., 2009).

Sanjay *et al*. (2012) conducted a CFD study on a UCAV configuration consisting of a moderately swept, tailless, flying wing with a cranked trailing edge. This was

designed for low observability in hostile environments rather than high manoeuvrability, for reasons of survivability. CFD allows observation of the vortex flow in the wake of the flying UCAV. Aerodynamic studies were also carried out in a wind tunnel using different angles of attack. CFD data obtained using STAR CCM+ CFD code was compared to experimental wind tunnel results. Flow visualization provides insights into UCAV manoeuvrability, since it allows analysis to be made of vortex bursting in relation to aerodynamic lift under steady and unsteady conditions. The CFD analysis was carried out over 2–3000 iterations to attain convergence, and steady pressure and velocity distributions and lift and drag forces. In the computational domain with a tetrahedral mesh, the walls were positioned to effectively capture the turbulence flow around the UCAV and generate a realistic solution. To effectively capture the turbulence above the UCAV model, five prism layers of 18 mm were used. A tetrahedral surface mesher was used to mesh the entire geometry. An element size of 0.5 mm was maintained over the UCAV model to capture the exact geometry and critical regions. The outer domain was meshed with a tetrahedral mesh of an element size of 55 mm.

Successful application of turbulence models has greatly increased the quality of numerical simulations. Turbulence in a flow becomes dominant over all other flow phenomena. The complexity of turbulence models varies considerably depending on the amount of detail required in the numerical simulation. Complexity is due to the nature of the Navier–Stokes equation, which is a non-linear, time-dependent, three-dimensional partial differential equation.

One of the most prominent turbulence models, the (k-epsilon) model, is implemented in most general purpose CFD codes. The (k-epsilon) model is stable, numerically robust and accurate, and has excellent predictive capability. The first transported variable is turbulent kinetic energy (k) and the second is turbulent dissipation (ε), which determines the scale of the turbulence.

1.1.14 Further Reading

1 Azlin MA, Mat Taib CF, Kasolang S and Muhammad FH (2011). CFD analysis of winglets at low subsonic flow. *Proceedings of the World Congress on Engineering – Vol. I*. 6–8 July. London, United Kingdom.

2 Barbarino S, Bilgen O, Ajaj RM, Friswell MI and Inman DJ (2011). A review of morphing aircraft. *Journal of Intelligent Material Systems and Structures.* **22**: 823–877.

3 Boschetti PJ, Cárdenas EM and Amerio A (2012). Induced drag reduction of an airplane using local twist, panel method verification. *50th AIAA Aerospace Sciences Meeting*. 9–12 January. Nashville, Tennessee, pp. 1–10.

4 Cetinsoy E, Dikyar S, Hancer C, Oner KT, Sirimoglu E, Unel M and Aksit MF (2012). Design and construction of a novel quad tilt-wing UAV. *Mechatronics*. In press.

5 Cook MV, Buonanno A and Erbsloeh SD (2008). A circulation control actuator for flapless flight control. *The Aeronautical Journal.* **112**(1134): 483–489.

6 Gamboa P, Aleixo P, Vale J, Lau F and Suleman A (2007) Design and testing of a morphing wing for an experimental UAV. *Platform Innovations and System Integration*

for Unmanned Air, Land and Sea Vehicles (AVT-SCI Joint Symposium). Neuilly-sur-Seine, France, pp. 17–1–17-30.
7 Kroo I, Prinz F and Eaton J (2003). UAV aeroelastic control using redundant micro-actuators. Techical report, AFOSR. Arlington, VA.
8 Park K, Han J, Lim H, Kim B, and Lee J (2008). Optimal design of airfoil with high aspect ratio in unmanned aerial vehicles. *International Journal of Aerospace and Mechanical Engineering.* **2**(1): 66–72.
9 Phillips WF (2005). New twist on an old wing theory. *Aerospace America*. **January**: 27–30.
10 Reneaux J, Thibert JJ and Rodde AM (1997). Airfoil design for sailplanes and ultralight aircraft. *XXV OSTIV Congress*. 3–11 July. Saint-Auban sur Durance. France, pp. 1–7.
11 Ma R, Zhong B, Liu P and Drikakis D (2010). Multi-objective optimization design of low Reynolds-number airfoils S1223. *27th International Congress of the Aeronautical Sciences*. 19–24 September. Nice. France.
12 Sanchez A, García-Carrillo LR, Rondon E, Lozano R and Garcia O (2011). Hovering flight improvement of a quad-rotor mini UAV using brushless DC motors. *Journal of Intelligent and Robotic Systems.* **61**(1–4): 85–101.
13 Shyy W, Klevebring F, Nilsson M, Sloan J, Carroll B and Fuentes C (1999). Rigid and flexible low Reynolds number airfoils. *Journal of Aircraft.* **36**(3): 523–529.
14 Syed HM, Hameed MS and Manarvi IA (2011). A review of swept and blended wing body performance utilizing experimental, FE and aerodynamic techniques. *International Journal of Research and Reviews in Applied Sciences.* **8**(3): 371–385.
15 Tianyuan H and Xiongqing Y (2009). Aerodynamic/stealthy/structural multidisciplinary design. *Chinese Journal of Aeronautics.* **22**: 380–386.
16 Wilbur ML and Wilkie WK (2005). Active-twist rotor control applications for UAVs. *Proceedings of the 24th Army Science Conference.* 29 November–2 December. Orlando, Florida, pp. 1–8.
17 Wisnoe W, Nasir RE, Kuntjoro W and Mamat AM (2009). Wind tunnel experiments and CFD analysis of blended wing body (BWB) unmanned aerial vehicle (UAV) at Mach 0.1 and Mach 0.3. *13th International Conference on Aerospace Sciences and Aviation Technology*. 26–28 May. Cairo, Egypt.
18 Xiaoping X, Xiaoping Z, Zhou Z and Ruijun F (2011). Application of active flow control technique for gust load alleviation. *Chinese Journal of Aeronautics.* **24**: 410–416.
19 Yang S, Han J and Lee I (2006). Characteristics of smart composite wing with SMA actuators and optical fiber sensors. *International Journal of Applied Electromagnetics and Mechanics.* **23**: 177–186.

1.1.15 Problems

Problem 1

Using the data in Table 1.1, plot the mean camber line for the NACA 2412 airfoil. Identify the chordwise location of the maximum camber.

Table 1.1 Mean camber line ordinates for the NACA 2414 airfoil.

x coordinate	Mean camber line
0.000	0.000
0.013	0.003
0.025	0.004
0.050	0.006
0.075	0.008
0.100	0.009
0.150	0.013
0.200	0.015
0.250	0.017
0.300	0.019
0.400	0.020
0.500	0.020
0.600	0.018
0.700	0.015
0.800	0.011
0.900	0.006
0.950	0.003
1.000	0.000

Problem 2

Using the Kutta–Joukowski theorem, calculate the circulation (Γ) and the lift per unit span (L') for a thin symmetric airfoil of chord (c) of 0.70 m, at angles of attack (α) of 5° and 10° in a standard atmosphere with air density (ρ_∞) of 1.225 kg/m^3 and airflow velocity (V_∞) of 40 m/s; see Eqs. (1.5) and (1.6).

$$\Gamma = \pi \alpha c V_\infty \tag{1.5}$$

$$L' = \rho_\infty V_\infty \Gamma = \pi \alpha c \rho_\infty V_\infty^2 \tag{1.6}$$

Problem 3

Calculate Γ and L' for a thin cambered airfoil of c = 0.70 m, at α of 5° and 10°, in standard atmosphere and V_∞ of 50 m/s. The Fourier coefficients are $A_0 = \alpha - 0.004517$ and A_1 = 0.08146; Eqs. (1.7) and (1.8).

$$\Gamma = cV_\infty \left(\pi A_0 + \frac{\pi}{2} A_1 \right) \tag{1.7}$$

$$L' = \rho_\infty V_\infty \Gamma = \rho_\infty V_\infty^2 c\pi = \left(A_0 + \frac{1}{2} A_1 \right) \tag{1.8}$$

Problem 4

Estimate the laminar boundary-layer thickness (δ_L) at the trailing edge for a chord length of 0.9 m, the net laminar skin-friction drag coefficient ($C_{f\mathrm{L}}$), the turbulent boundary layer thickness (δ_T) at the trailing edge, and the net turbulent skin-friction drag coefficient ($C_{f\mathrm{T}}$), for a thin airfoil. The chord-length Reynolds number ($\mathrm{Re_c}$) and chord-length Reynolds number based on distance x from the leading edge (Re_x) are (2×10^6); Eqs. (1.9)–(1.12).

$$\delta_{\mathrm{L}} = \frac{5c}{\sqrt{\mathrm{Re_c}}} \tag{1.9}$$

$$C_{f\mathrm{L}} = 2\frac{1.328}{\sqrt{\mathrm{Re_c}}} \tag{1.10}$$

$$\delta_{\mathrm{T}} = \frac{0.37x}{\mathrm{Re}_x^{1/5}} \tag{1.11}$$

$$C_{f\mathrm{T}} = 2\frac{0.074}{\mathrm{Re_c}^{1/5}} \tag{1.12}$$

Problem 5

A wing of $\mathrm{AR}_1 = 5$ and $\alpha_1 = 4°$ has a lift coefficient (C_{L}) of 1.0. Calculate the α_2 at which two wings of $\mathrm{AR}_2 = 8$ and 9 will have to operate to generate the same C_{L}; Eq. (1.13).

$$\alpha_2 = \alpha_1 + \frac{C_L}{\pi}\left(\frac{1}{\mathrm{AR}_2} - \frac{1}{\mathrm{AR}_1}\right) \tag{1.13}$$

Problem 6

An airfoil has $c_l = 0.0$ at $\alpha = -1°$ and $c_l = 0.8$ at $\alpha = 6°$. Calculate the airfoil lift slope (a_0) and the wing lift slope (a) for a wing of AR = 7.5. The lift efficiency factor (τ) is 0.09; Eqs. (1.14) and (1.15).

$$a_0 = \frac{c_{l2} - c_{l1}}{\alpha_2 - \alpha_1} \tag{1.14}$$

$$a = \frac{a_0}{1 + \left(\dfrac{a_0}{\pi \mathrm{AR}}\right)(1+\tau)} \left(\text{a and } \mathrm{a}_0 \text{ are per radian}\right) \tag{1.15}$$

Problem 7

Calculate a for a low-AR straight wing of AR = 3.5; Eq. (1.16).

$$a = \frac{a_0}{\sqrt{1 + \left(\dfrac{a_0}{\pi \mathrm{AR}}\right)^2} + a_0 / (\pi \mathrm{AR})} \tag{1.16}$$

Problem 8

The zero-lift angle of attack (α_{L0}) for the NACA 23012 airfoil is given by Eqs. (1.17) and (1.18). Compute α_{L0}.

$$\alpha_{L0} = -\frac{1}{\pi}[-2.8683\theta + 3.0576\sin\theta - 2.1843\sin\theta\cos\theta + 0.665\sin\theta(cos^2\theta + 2)]_0^{0.9335} \quad (1.17)$$

and

$$-\frac{1}{\pi}[0.02208\theta - 0.02208\sin\theta]_{0.9335}^{\pi} \quad (1.18)$$

1.2 UAV Flight Stability and Control

'The balancing of a gliding or flying machine is very simple in theory. It merely consists in causing the center of pressure to coincide with the center of gravity. But in actual practice there seems to be an almost boundless incompatibility of temper which prevents their remaining peaceably together for a single instant, so that the operator, who in this case acts as peacemaker, often suffers injury to himself while attempting to bring them together.'

Wilbur Wright

CONTENTS

1.2.1 Introduction – Flight Stability

Stability is defined as the tendency of the UAV to return to a condition of equilibrium when subjected to a disturbance in flight. This is typically caused by gusts or flight-control input (Nelson, 1998). *Static stability* is the initial response of the aircraft to regain equilibrium upon a disturbance. It can take be positive, negative, divergent or neutral. *Dynamic stability* refers to the response of the system over time. Even when an aircraft has inherent positive static stability, it usually tends to overshoot the equilibrium condition, producing a series of oscillations. If the magnitude of successive oscillations becomes smaller over time, the system has positive dynamic stability. When the time history of dynamic oscillations is short, the system is said to be highly damped. When oscillations take longer, the system is considered lightly damped. An aircraft with positive static stability but no damping continues to oscillate without experiencing any

decrease in the amplitude of the oscillations; such an aircraft has neutral dynamic stability. The location of the centre of gravity (CG) that would cause the aircraft to have neutral static longitudinal stability is called the *neutral point* (NP). Moving the CG forward of the NP gives positive static stability, and moving the CG aft of the NP makes the aircraft statically unstable. A necessary condition for positive static longitudinal stability is, therefore, that the CG is forward of the NP. This criterion is stated in terms of the aircraft's *static margin* (SM), which is a non-dimensional measure of the aircraft's stability. A large SM implies a very stable but not particularly manoeuvrable aircraft. Highly manoeuvrable UAVs have a short positive SM. Vehicles with zero or negative SM require a computer fly-by-wire flight control system for flight control.

1.2.2 Control Surfaces

Conventional aircraft control surfaces produce the moments that cause rotations in pitch, roll and yaw. *Elevators* and *stabilators* generate a lift force at the aircraft's tail. The moment arm of this force from the aircraft's CG generates a pitching moment (Nelson, 1998). *Ailerons* deflect differentially and create more lift on one wing than the other, and therefore a net rolling moment. The *rudder* deflects to generate a lift force in a sideways direction. This force acts at a distance from the aircraft's CG, producing a moment about the vertical axis that causes the aircraft to yaw.

UAVs represent unique aircraft configurations, in that they employ novel types of hinged control surfaces. Often, the functions of two control surfaces are combined in a single surface. The names of these controls are a combination of the names of the two surfaces. A stabilator combines the functions of the horizontal stabilizer and the elevator in an 'all-moving' control surface. *Canard stabilators* are placed forward of the wings. A *flaperon* combines the functions of a plain flap and an aileron. *Elevons* combine elevators and ailerons, deflecting together to function as elevators for pitch control and also moving differentially, like ailerons, to provide roll control. In a V-tail UAV, the moveable control surfaces of the tail are called *ruddervators* (Figure 1.8). These function as rudders when moving differentially and as elevators when moving together.

1.2.3 Principles of Aircraft Stability

During flight, moments on a UAV are created by the aerodynamic load distribution and the thrust force not acting through the CG. Aerodynamic moments are expressed in terms of the dimensionless coefficients for pitching moment (C_{m}), rolling moment (C_{ℓ}) and yawing moment (C_{n}). For airplane configurations, the characteristic length (l) is the mean chord (c) for the pitching moment and the wing span (b) for the rolling and yawing moments. The values of C_{m}, C_{ℓ} and C_{n} depend on the angle of attack (α), Reynolds number (Re), Mach number (M) and sideslip angle (β) and are functions of the angular rates and sideslip of the aircraft (Nelson, 1998). Figure 1.9 shows the definition of velocities, forces and moments.

UAVs designed with inherent aerodynamic stability possess satisfactory handling or flying qualities. In contrast, UCAVs are purposely designed with limited stability in the interest of manoeuvrability in combat operations and require complex control management and electromechanical stability augmentation systems.

A UAV, particularly if in a single-main-rotor helicopter configuration, can be statically stable but dynamically unstable (Austin, 2010). However, to be dynamically stable

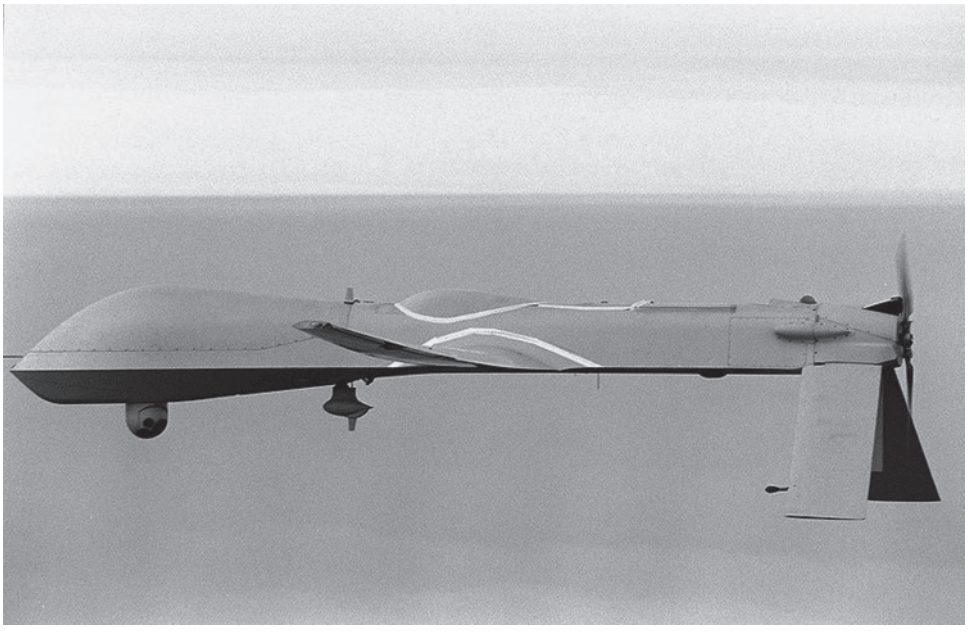

Figure 1.8 Down-angled ruddervators in an RQ-1 Predator. Photo: US Navy.

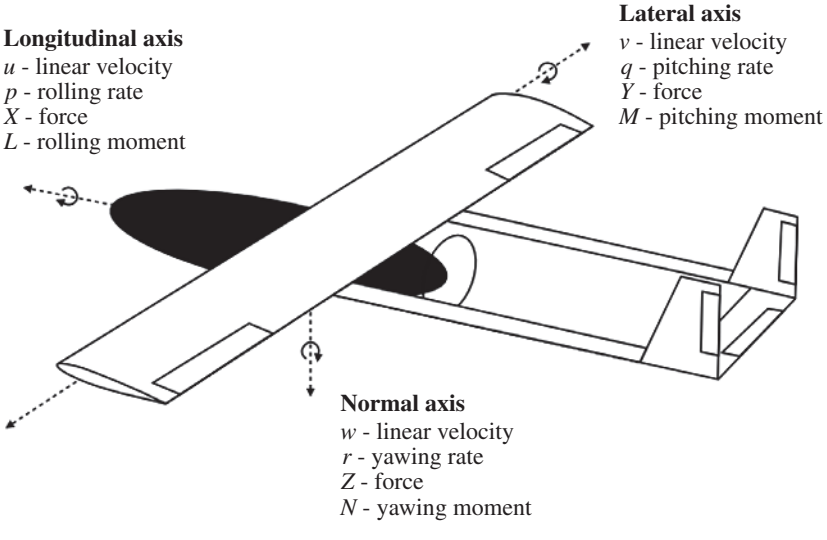

Figure 1.9 Definitions of translational and angular velocity, and aerodynamic forces and moments.

it is a necessary condition that the aircraft is statically stable. Dynamic stability entails damped oscillatory motion, whereby the oscillations caused by the disturbance are gradually dissipated by inertial and aerodynamic forces that oppose the motion of the vehicle. The measures of dynamic stability are the frequency and period of the oscillations, and the time it takes to damp the undesirable oscillatory motion to half of

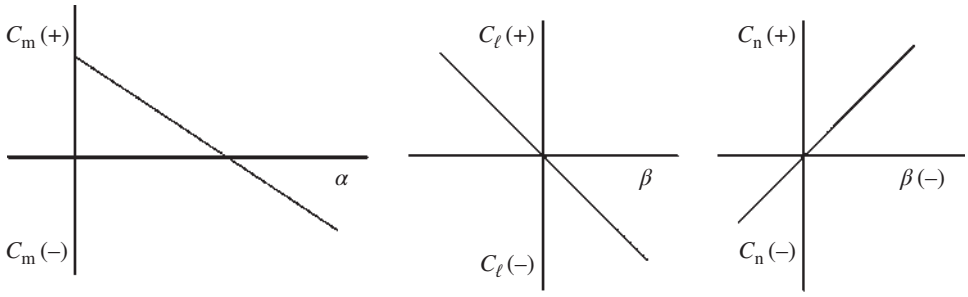

Figure 1.10 Stable longitudinal (in pitch), lateral (in roll) and directional (in yaw) conditions.

its amplitude (Nelson, 1998). A necessary condition for longitudinal static stability of the UAV is that the pitching moment curve has a negative slope through the equilibrium point. Also, to trim the vehicle at a positive α and produce useful lift, the C_m at $\alpha = 0°$ must be greater than zero. The slope must be negative for lateral static stability and positive for directional static stability (see Eq. (1.19) and Figure 1.10).

$$\text{pitch}\ \frac{dC_m}{d\alpha} < 0 \quad \textit{roll}\ \frac{dC_\ell}{d\beta} < 0 \quad \text{yaw}\ \frac{dC_n}{d\beta} > 0 \tag{1.19}$$

1.2.4 UAV Configurations

In an orthodox tail-aft airplane configuration, the principal contributor to stability in pitch is the horizontal stabiliser in a *longitudinal dihedral* arrangement. However, the wing, fuselage and propulsion thrust also play a part (Nelson, 1998). A wing constructed using a conventional airfoil is destabilising in pitch, since such airfoils exhibit a negative nose-down moment. A positive pitching moment about the AC of the wing is achieved using a reflexed airfoil. The major contributor to stability in roll is the wing dihedral. Wing sweep, wing position on the fuselage and the vertical fin also influence the restoring roll moment.

The wing and fuselage are destabilizing in yaw, and directional stability is primarily attained by the vertical tail. Nonetheless, horizontal-takeoff-and-landing (HTOL) UAVs come in diverse airframe configurations, including, for example, canard, tailless, flying wing and delta wing (Austin, 2010). VTOL vehicles can have co-axial rotor, tandem rotor and quad rotor designs, and hybrid UAVs can use tilt-rotor, tilt-wing, tilt-wing-body, ducted fan and other designs. Flight stability in pitch in orthodox and unconventional vehicle configurations is achieved by methods that are specific to each category.

Orthodox layout: The aircraft's CG is located at the AC of the wing. The wing's camber produces a nose-down pitching moment. The tailplane generates a download to balance the wing's moment. An additional lift force must be developed by the wing to compensate for the tailplane download. For highly cambered wings, the tail's download must be larger. The horizontal stabiliser operates in the vortex-induced downwash of the wing and should consequently be set at a slightly negative angle relative to the local airflow in a *longitudinal dihedral* configuration, so that the tail

generates the required downforce. The elevator modifies the tailplane's camber and adjusts the tailplane's download for different flight conditions.

Canard configuration: A canard foreplane is free from interference from the main wing downwash and the propeller slipstream. Unlike the aft-tail configuration, which yields a download, the canard foreplane produces lift to counteract the nose-down moment and adds to the total lift generated by the wing. Canard control works effectively to trim the additional nose-down moment originated by high-lift devices in the wing, such as flaps. However, a canard configuration reduces the vehicle's static stability. This is because any lifting surface located ahead of the CG moves the NP forward. In a canard, the foreplane causes the NP to lie ahead of the wing's AC. To enhance stability, a canard UAV must have the CG forward, and therefore the foreplane carries the camber-induced pitching load and an additional load caused by the forward position of the CG. The canard lies in the vortex-induced upwash of the wing. However, the forewing produces downwash that influences the α of the wing. The downwash can be reduced using a small forewing of large AR.

Tailless aircraft: Flying wing, delta, double delta, and lambda UAV configurations achieve longitudinal stability using wing sweepback and washout (Figure 1.11). The aircraft's CG is positioned ahead of the AC and the wingtips produce a download. A wing with reflex camber helps give a neutral pitching moment.

In the orthodox layout, stability in roll is primarily achieved using the wing dihedral, which in UAVs takes different forms such as elliptical, polyhedral, gull, and inverted gull dihedral. Typically, high-wing UAVs have no dihedral and the wing is therefore neutrally stable in roll (Nelson, 1998). As the aircraft rolls, the down-going wing meets the freestream at a greater α. At the same time, the α of the up-going wing is reduced. The rolling movement is therefore damped out, but there is no tendency to correct the banked attitude of the vehicle once the roll has stopped. The increase in lift force on the

Figure 1.11 Northrop Grumman X-47B UCAS-D. Photo: Rob Densmore. (*See insert for color representation of this figure.*)

down-going wing also increases the strength of the wingtip vortex creating a drag force that tends to yaw the aircraft. Thus there is cross-coupling of the rolling and yawing motions. The fin surface area (S) and its distance from the aircraft's CG are important considerations in obtaining adequate stability in yaw.

1.2.5 Relaxed Stability

For use in windy and harsh flight environments, it is desirable to reduce the response of some UAVs to turbulence in order to maintain payload sensors on the target (Austin, 2010). Strong inherent aerodynamic stability, large S and high AR in relation to the vehicle's mass cause UAVs to exhibit high responses to atmospheric turbulence. Near-neutral flight stability ensures the minimum disturbance from air turbulence. However, an automatic flight control and stability system (AFCS) is often required to ensure that the vehicle has positive spatial stability that will prevent the aircraft wandering off course.

1.2.6 Case Study

Cardenas *et al*. (2009) evaluated the static stability and open-loop dynamic stability of a small airplane designed for ecological conservation. The small UAV is a twin-boom, pusher-propeller configuration with maximum takeoff mass of 182 kg and a payload of 40 kg consisting of a high-technology camera that is used to find oil leakages. The wing is of rectangular planform, straight with local twist, and has no dihedral. The b is 5.2 m, AR is 8.57 and S is 3.13 m^2. The wing uses an NACA 4415 airfoil along the complete wingspan and Re is 1.41×10^6. Flight stability derivatives were computed using Tornado, an open-source 3D vortex lattice program with application of inviscid CFD.

Longitudinal stability was evaluated as a function of α, elevator deflection angle (δ_e) and q. The wing lift coefficient (C_L) for $\alpha = 0°$ and $\delta_e = 0°$ is 0.51, which increases to $C_L = 0.62$ for $\delta_e = 10°$. The wing lift slope (a) is 5.46 rad^{-1}. The C_L varies with δ_e by 0.68 rad^{-1}. Longitudinal stability was assessed using C_m curves at various δ_e. The C_m at $\alpha = 0°$ is 0.015 and the C_m slope is $-2.73\ rad^{-1}$, whereby the negative sign indicates that the aircraft is inherently statically stable in pitch. The C_m slope increases to $-2.87\ rad^{-1}$ for $\delta_e = 10°$. The aircraft's CG is located at 0.25 c and the NP is positioned at 0.75 c.

The lateral-directional static stability coefficients were studied as a function of sideslip angle, rudder and aileron deflections, and yaw and roll rates at $\alpha = 0°$. The variation of side force coefficient with sideslip angle ($C_Y\beta$) has a derivative of $C_Y\beta = -0.56\ rad^{-1}$ and the slope is $-0.017\ rad^{-1}$. Thus, the negative sign indicates that the airplane is inherently laterally stable. The aircraft is also directionally stable with a positive slope of $0.155\ rad^{-1}$. The variation in side force coefficient with rudder angle ($C_Y\delta_r$) has a derivative $C_Y\delta_r = -0.27\ rad^{-1}$; the yawing ($C_n\delta_r$) and roll moment ($C_\ell\delta_r$) coefficients due to the deflection of the rudder were determined and their derivatives were $C_n\delta_r = 0.149\ rad^{-1}$ and $C_\ell\delta_r = -0.006\ rad^{-1}$ at the zero sideslip condition. The variation in rolling coefficient with aileron angle ($C_\ell\delta_a$) is $C_\ell\delta_a = -0.206\ rad^{-1}$. Increasing the aileron angle increases the roll moment. The variation in yawing coefficient with aileron angle ($C_n\delta_a$) has a derivative $C_n\delta_a = 0.017\ rad^{-1}$ and the side force variation with aileron angle ($C_Y\delta_a$) is $C_Y\delta_a = -0.001\ rad^{-1}$. The rolling ($I_\ell$), pitching ($I_M$) and yawing ($I_n$) moments of inertia of the UAV are $I_\ell = 150\ kgm^2$, $I_M = 400\ kgm^2$ and $I_n = 400\ kgm^2$, based on mass distribution.

Table 1.2 Characteristics of dynamic stability in pitch.

	Short-period mode	Phugoid mode
Period (T), s	2.05	26.04
Time to half amplitude ($t_{1/2}$), s	0.34	191.67
Number of cycles to half amplitude ($N_{1/2}$), cycles	0.17	7.36
Damping ratio (ζ)	0.551	0.015
Undamped natural frequency (ω_n), rad/s	3.68	0.24

The static stability data obtained using the vortex-lattice method are used to determine the airplane dynamic stability response characteristic (Table 1.2). The two longitudinal modes of motion – the short-period mode ($\lambda_{1,2}$) and the phugoid mode ($\lambda_{3,4}$) – were $\lambda_{1,2} = -2.025 \pm 3.070i$) and $\lambda_{3,4} = -0.004 \pm 0.241i$. The negative values of the longitudinal modes indicate that the UAV is dynamically stable. On a sudden disturbance, the response would decay sinusoidally over time.

1.2.7 Further Reading

1 Austin R (2010). *Unmanned Aircraft Systems: UAV Design, Development and Deployment*. John Wiley & Sons, Chichester.
2 Cárdenas EM, Boschetti PJ and Amerio A (2009). Stability and flying qualities of an unmanned airplane using the vortex-lattice method. *Journal of Aircraft.* ***46***(4): 1461–1464.
3 Johnson EN, Chowdhary G, Chandramohan R and Calise AJ (2011). UAV flight control using flow control actuators. *AIAA Flight Mechanics Conference*, Portland Oregon. pp. 1–6.
4 Lungu M (2012). Stabilization and control of a UAV flight attitude angles using the Backstepping method. *World Academy of Science, Engineering and Technology.* ***61***: 290–297.
5 Nelson RC (1998). *Flight stability and Automatic Control*. McGraw Hill, New York.
6 Salih AL, Moghavvemi M, Mohamed HA and Gaeid KS (2010). Flight PID controller design for a UAV quadrotor. *Scientific Research and Essays.* ***5***(23): 3660–3667.
7 Uhlig DV and Selig MS (2011). Stability characteristics of micro air vehicles from experimental measurements. *29th AIAA Applied Aerodynamics Conference*. 27–30 June. Honolulu. Hawaii, pp. 1–13.

1.2.8 Problems

Problem 1

Figure 1.12 depicts a low-wing UAV configuration and the contributions of the wing and tail to static stability. The geometry and aerodynamics of the vehicle are shown in Table 1.3. A necessary condition for static stability is that $C_{m\alpha} < 0$, and $C_{m0} > 0$ is required to obtain useful lift and longitudinal trim at $\alpha > 0°$. Calculate the contribution

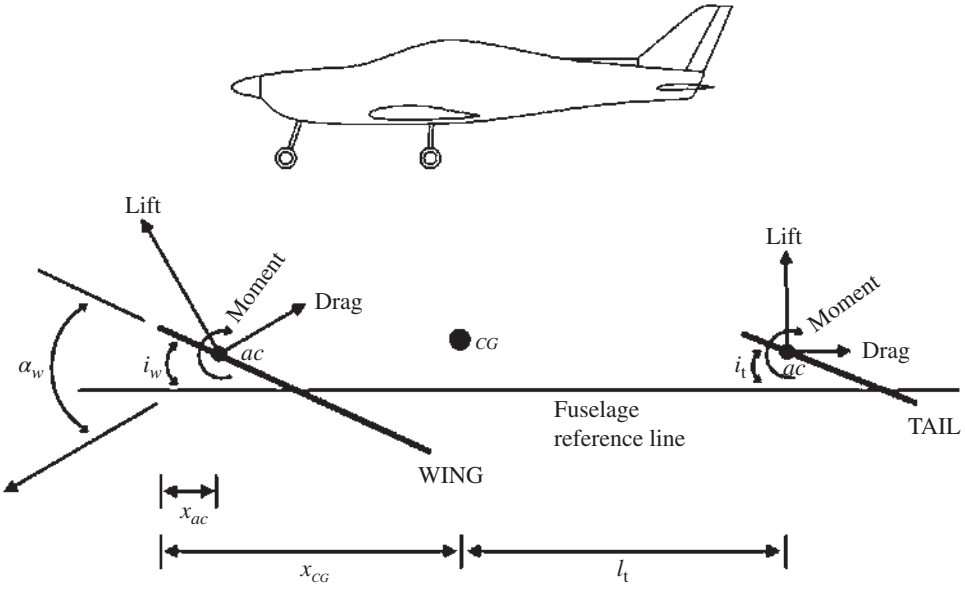

Figure 1.12 Low-wing UAV configuration and stability definitions.

Table 1.3 Vehicle geometry and aerodynamic characteristics.

Aircraft	Geometry	Wing airfoil	Tail airfoil
Mass = 200 kg	b = 5 m	$i_w = 1.0°$	$i_t = -1°$
V_{max} = 40 m/s	mean c = 0.62 m	$c_{l\alpha w}$ = 0.092/deg	$c_{l\alpha t}$ = 0.015/deg
	AR_w = 8.6	c_{macw} = −0.115	c_{mact} = 0
	S_w = 3.1 m^2	$x_{ac} = 0.25c$	
	S_t = 0.72 m^2	$\alpha_0 = -3°$	
	l_t = 2.4 m		

of the *wing* to static stability of the vehicle ($C_{m\alpha w} < 0$); Eqs. (1.4)–(1.7). Is the moment stabilizing or destabilizing?

The notation used is as follows:

Aircraft

C_{m0} = aircraft moment coefficient at α = 0°
$C_{m\alpha}$ = aircraft moment curve slope
V_{max} = aircraft maximum cruise velocity

Wing

AR_w = aspect ratio of the wing planform
b = wing span

$\bar{c}$ = wing mean aerodynamic chord
C_{macw} = wing moment about the aerodynamic centre
c_{macw} = wing airfoil moment about the aerodynamic centre
C_{mcgw} = wing contribution to moment about aircraft's centre of gravity
C_{m0w} = wing moment at $\alpha = 0°$
$C_{m\alpha w}$ = wing moment curve slope
C_{Lw} = wing lift coefficient
C_{L0w} = wing lift coefficient at $\alpha = 0°$
$C_{L\alpha w}$ = wing lift curve slope
$c_{L\alpha w}$ = wing airfoil lift curve slope
$C_{l\alpha w}$ = wing lift curve slope (per radian)
i_w = wing incidence angle (mean chord to fuselage)
S_w = wing surface area
x_{ac} = distance from wing leading edge to aerodynamic centre
α = angle of attack
α_0 = zero-lift angle of attack of wing airfoil
α_{0w} = wing zero-lift angle relative to fuselage reference line

Tail

AR_t = aspect ratio of the tail planform
$C_{L\alpha t}$ = tail lift curve slope
$c_{L\alpha t}$ = tail airfoil lift curve slope
C_{mact} = tail moment about the aerodynamic centre
c_{mact} = tail airfoil moment about the aerodynamic centre
$C_{m\alpha t}$ = tail moment curve slope
C_{m0t} = tail moment at $\alpha = 0°$
i_t = tail incidence angle
l_t = tail moment arm
S_t = horizontal tail surface area
V_H = horizontal tail volume ratio
α = tail angle of attack
ε = downwash incidence angle
ε_0 = downwash angle at tail when wing is at $\alpha = 0°$
η = ratio of tail to wing dynamic pressures (tail efficiency)

Fuselage

C_{maf} = fuselage moment curve slope
C_{m0f} = fuselage moment at $\alpha = 0°$
$k_2 - k_1$ = correction factor for body fineness ratio
l_f = fuselage length
w_f = average width of fuselage sections
x = coordinate
Δx = length of fuselage increments
ε_u = local induced angle due to upwash or downwash at each fuselage segment

Neutral point

x_{NP} = neutral point
The equations used are as follows:

Wing lift curve slope:

$$C_{L\alpha w} = \frac{C_{l\alpha w}}{1 + C_{l\alpha w} / \left(\pi AR_w\right)} \text{ in radians} \tag{1.20}$$

Wing moment coefficient at $\alpha = 0°$:

$$C_{m0w} = C_{macw} + C_{L0w}\left(\frac{x_{CG}}{\bar{c}} - \frac{x_{ac}}{\bar{c}}\right) \tag{1.21}$$

Wing moment curve slope:

$$C_{m\alpha w} = C_{L\alpha w}\left(\frac{x_{cg}}{\bar{c}} - \frac{x_{ac}}{\bar{c}}\right) \tag{1.22}$$

Wing lift coefficient at $\alpha = 0°$:

$$C_{L0w} = C_{L\alpha w}\left|\alpha_0\right| \tag{1.23}$$

Problem 2
The contribution of the tail to the static stability of the vehicle ($C_{m\alpha t} < 0$) is achieved by careful adjustment of V_H and $C_{L\alpha t}$. The $C_{L\alpha t}$ can be adjusted by modifying the tail AR_t. For the UAV in Problem 1, calculate the contribution of the *tail* to static stability using Eqs. (1.24)–(1.29). Is the moment stabilizing or destabilizing?

The following equations are used:

Tail moment coefficient at $\alpha = 0°$ (intercept):

$$C_{m0t} = \eta V_H C_{L\alpha t}\left(\varepsilon_0 + i_w - i_t\right) \quad \eta \text{ assumed to be unity} \tag{1.24}$$

Tail moment curve slope:

$$C_{m\alpha t} = -\eta V_H C_{L\alpha t}\left(1 - \frac{d\varepsilon}{d\alpha}\right) \tag{1.25}$$

Tail volume ratio:

$$V_H = \frac{l_t S_t}{S_w \bar{c}} \tag{1.26}$$

Downwash angle in radians:

$$\varepsilon = \frac{2C_{Lw}}{\pi AR_w} \tag{1.27}$$

Downwash angle at tail when wing is at $\alpha = 0°$:

$$\varepsilon_0 = \frac{2C_{L0w}}{\pi AR_w} \tag{1.28}$$

Downwash slope:

$$\frac{d\varepsilon}{d\alpha} = \frac{2C_{L\alpha w}}{AR_w} \quad C_{L\alpha w} \text{ is in radians} \tag{1.29}$$

Problem 3

For the UAV in Problem 1, calculate the contribution of the *fuselage* to static stability ($C_{m\alpha f}$) using Eqs. (1.30)–(1.34) (Multhopp's method). Is the moment stabilizing or destabilizing?

$$C_{m0f} = \frac{k_2 - k_1}{36.5S_w\overline{c}} \sum_{x=l_f}^{x=0} w_f^2 \left(\alpha_{0w} + i_f\right)\Delta x \tag{1.30}$$

$$C_{m\alpha f} = \frac{1}{36.5\overline{S_w}c} \sum_{x=l_f}^{x=0} w_f^2 \frac{\partial \varepsilon_u}{\partial \alpha}\Delta x \qquad \left(deg^{-1}\right) \tag{1.31}$$

given the following equations:

Correction factor for body fineness ratio:

$$k_2 - k_1 = 0.84 \tag{1.32}$$

Summation of individual fuselage segments:

$$\sum_{x=l_f}^{x=0} w_f^2 \left(\alpha_{0w} + i_f\right)\Delta x = -400 \tag{1.33}$$

Summation of individual fuselage segments:

$$\sum_{x=l_f}^{x=0} w_f^2 \frac{\partial \varepsilon_u}{\partial \alpha}\Delta x = 35 \tag{1.34}$$

Problem 4

Compute the stick-fixed NP for the vehicle in Problem 1 using Eq. (1.35).

$$\frac{x_{NP}}{\overline{c}} = \frac{x_{ac}}{\overline{c}} - \frac{C_{m\alpha f}}{C_{L\alpha w}} + \eta V_H \frac{C_{L\alpha t}}{C_{L\alpha w}}\left(1 - \frac{d\varepsilon}{d\alpha}\right) \tag{1.35}$$